SINFONIA

Project title: Radiation risk appraisal for detrimental effects from medical exposure during management of patients with lymphoma or brain tumour (SINFONIA)

Grant Agreement: 945196

Call identifier: NFRP-2019-2020

Topic: NFRP-2019-2020-14 Improving low-dose radiation risk appraisal in medicine

Deliverable D2.2 - Software tool on personalised dosimetry in PET-CT and deep learning-guided algorithms for automated construction of computational models

Lead partner:	UNIGE (11)
Author(s):	Yazdan Salimi, Azadeh Akhavanallaf, Zahra Mansouri, Habib Zaidi
Work Package:	2
Delivery as per Annex I:	Month 30 (30.04.2023)
Actual delivery:	Month 30 (30.04.2023) Version 1; Month 39 (13.11.2023) – Version 2
Type:	Report
Dissemination level:	Public

Table of Contents

Abbreviations

CT: Computed Tomography

SPECT: Single-Photon Emission Computed Tomography

MC: Monte-Carlo

OAR: Organ at Risk

DL: Deep Learning

AI: Artificial Intelligence

List of figures

List of tables

1. Introduction

1.1 Radiation dosimetry in hybrid nuclear medicine imaging

Nuclear medicine (NM) protocols offer valuable diagnostic functional information by administration of the radiopharmaceuticals. The information about the pharmacokinetic and pharmacodynamic of specific targeted tracers can help diagnosing wide range of pathologies such as oncology to cardiac and brain disorders. Besides,

the therapeutic application of NM has proven to be an effective treatment for different malignant and benign disorders such as benign thyrotoxicosis and joint inflammation and various malignant tumours targeted therapies like prostate and neuroendocrine tumours. Acquiring structural images rich with anatomical information such as Computed Tomography (CT) can improve the diagnostic value of nuclear medicine tomographic procedures of SPECT and PET, at the same time increases the radiation dose burden to patient (1, 2). The dose imposed to patient is addition of two compartment of internal and external exposure due to the radiotracer and the CT tube radiation, respectively. Dose calculation for each of these components are prone to multiple uncertainties at multiple steps. Personalized radiation dose measurement is a crucial step in optimizing the patient-specific risk estimation. To yield the personalized internal dosimetry workflow, a personalized time-integrated activity, computational phantom, and dose transport system is required. On the other hand to calculate the personalized radiation dose in CT, a patient-specific computational phantom, scanner-specific calibration information, and acquisition specific exposure and geometry information is required. The available patient-specific radiation dosimetry pipelines are time-consuming and labour-intensive and needs special skills to be implemented. In this part of project, we aimed to develop methodologies, mainly through machine learning algorithms to remove the burdens of implementing patient-specific dosimetry in the clinical workflow, at the same time, tackle the uncertainties in dose calculations.

1.2 Personalized dosimetry and role of AI

1.2.1 Patient-specific computational phantoms (Organ segmentation)

Segmentation of healthy organs on Computed Tomography (CT) images is a critical and beneficial information in computational phantom generation, radiation therapy (RT) treatment planning (3) and other kinds of computer assisted applications such as pathologic detection (4, 5), prognosis prediction, image quantification (6), and radiation dosimetry. The manual segmentation of organs can be very time consuming, while the inter-observer and intra-observer variations was reported for segmentation tasks of healthy organs and tumoral tissues. Since the emergence of deep learning and machine learning in medical imaging especially medical image segmentation. In the way of reaching the personalized dosimetry in PET/CT we needed the patient-specific computational phantom which can be generated by organ segmentations. As a part of our project to reach this goal we developed a deep neural network to segment multiple healthy total-body organs (19 organs) with considering the accuracy and generalizability.

1.2.2 Internal personalized dosimetry

In current clinical nuclear medicine dosimetry, patient dose monitoring is commonly based on simplified models, such as those derived by the Medical Internal Radiation Dose Committee (MIRD) formalism (7). The traditional MIRD technique is based on organ-level dosimetry using time-integrated activity and radionuclide S-values, which represents the mean absorbed dose to a target organ per radioactive decay in a source organ. These quantitative parameters are modelled based on a reference computational model. This approach assumes a uniform activity distribution within each organ and ignores individual anatomical characteristics. To cope with inter-subject variability of anatomical features, the organ-level dosimetry approach was later extended by developing habitus-specific and patient-specific computational models (8, 9, 10, 11, 12). Furthermore, voxel-based dosimetry techniques have been developed, including dose point kernel (13) and voxel S-value (VSV) (7) approaches. Unlike probabilistic methods, dose point kernel is a deterministic approach that calculates the radial absorbed dose distribution around an isotropic point source in a homogeneous water medium (14, 15). Voxel-level MIRD schema is defined as a 3D voxel matrix representing the mean absorbed dose to a target voxel per unit activity in a source voxel embedded in an infinite homogeneous medium using Monte Carlo (MC) simulations. However, voxel-based dose calculation should in principle take into account non-uniform activity distribution of the radiotracer, the heterogeneity of the medium consisting of different material compositions, e.g. lung, soft tissue, and bone is ignored. In this regard, direct MC simulations, deemed the gold standard for implementation of a reliable dose calculation framework in clinical setting, enables accurate estimation of whole-body dose map (16, 17). Though MC simulation takes into account the non-uniform activity distribution and heterogeneity of patient-specific anatomical features, it suffers from expensive computational burden.
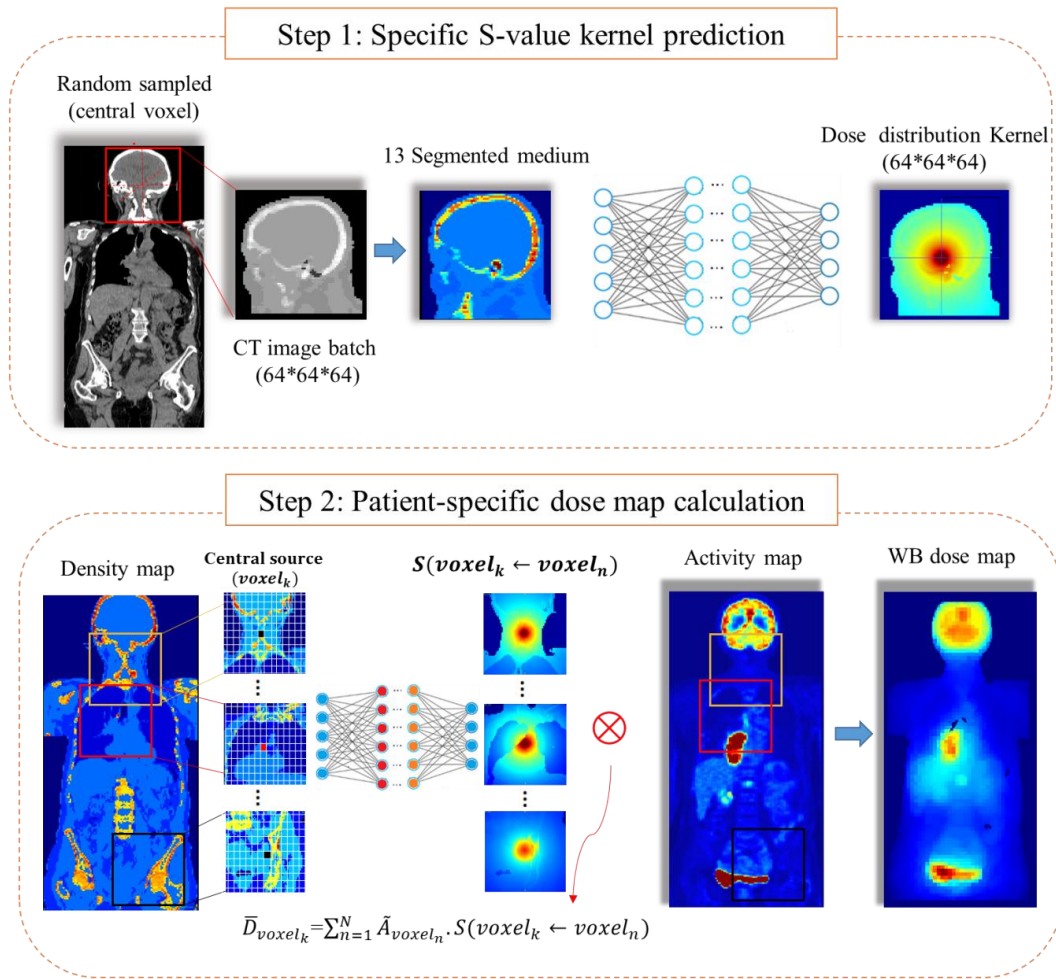
Figure 1. Schematic representation of the voxel-scale dosimetry procedure. The top and bottom panels show the deep learning-based specific S-value kernel prediction and MIRD-based voxel dosimetry formalism.

Accurate patient-specific dosimetry is becoming a must taking advantage of advances in targeted radionuclide therapy and theragnostic imaging (18). In personalized dosimetry, MC simulation is still considered the most accurate technique and the de facto reference standard for research application. Yet, this approach is not employed in routine clinical procedures owing to the heavy computational burden. Deep learning emerged as a promising technique in the area of computer vision and image processing, exhibiting superior performance over conventional state-of-the-art methods in medical images analysis. In this context, we developed a novel methodology to estimate whole-body dose distributions using a deep convolutional neural network, wherein unlike previous studies, generation of training datasets is no longer a bottleneck. The proposed dose map generation framework consists of two steps. In the first step, a deep neural network (DNN) is employed to predict dose distribution kernels, wherein the training dataset consists of only density maps obtained from CT images as input and the corresponding dose distribution kernel for a point source with unit activity obtained from MC simulations as output. In this approach, the simulation time for generating a ground truth (dose distribution map around the central voxel source) covering the annihilation photon mean free path is about 8000 times less than that required for whole-body MC simulations. This strategy makes it possible to provide a diverse and extensive training dataset. In addition, this approach would reduce the complexity of the training process as the DNN model should learn simpler features corresponding to a point source distribution compared to direct translation from hybrid density/activity maps to absorbed dose map. In the second step, specific dose distribution kernels predicted by the trained model are convolved with the activity map (here time-integrated activity from dynamic PET images) to generate the final whole-body dose map, in a manner analogous to the voxel-based MIRD formalism. The graphical abstract of the whole workflow is illustrated in **Figure 1**.

SINFONIA

D2.2 - Software tool on personalised dosimetry in PET-CT and deep learning-guided algorithms for automated construction of computational models

1.2.3 External personalized dosimetry scanner & Acquisition specific (Deep dose CT)

CT, one of the high-dose examinations, is responsible for a significant part of ionizing radiation exposure of patients (19, 20). The International Commission on Radiological Protection (ICRP) (21) suggested estimating the radiation dose delivered to patients from medical imaging procedures toward the optimization rule known as ALARA in order to minimize the risks through the appropriate use of ionizing radiation.

The recent emphasis on personalized medicine and patient-specific justification/optimization substantiates the critical demand to calculate specific parameters related to radiation risks (22, 23, 24, 25). The organ dose is a requirement for patient-specific dose calculation and has a good correlation with radiation risks (24). On the other hand, it has been shown that the radiation dose delivered to specific organs can reach the deterministic dose levels, especially in serial CT examinations (recurrent exposures), which is common practice in patients follow-up (26, 27, 28).

The estimation of organ doses can be performed using multiple methodologies. The most straightforward approach uses conversion factors specific to the scanning protocols. An alternative option is to use dedicated software tools, such as ImpactDose[1] and Radimetrics (29). Both above mentioned software packages proved to have a low correlation with organ doses calculated by more accurate Monte Carlo (MC) simulation tools using patient-specific or reference computational models (11, 30), particularly when the Tube Current Modulation (TCM) system is activated (31, 32, 33). While MC calculations using patient-specific computational models is deemed to be the most accurate approach and is often regarded as the gold standard technique, its downsides, including computational time, high computational burden, and required expertise in computer programming, limit its adoption in clinical setting. Exploiting the parallel computational power of GPUs enabled MC calculations to be faster and more suited for adoption in clinical setting (34, 35). Yet, the complexity associated with the technique remains a significant hurdle. Deep learning-based algorithms are currently used in various medical imaging applications, including image regression (36), registration (37), segmentation (38), radiation dosimetry calculation (39, 40), and optimization (41, 42). This part of our project aimed to develop a fully automated method to estimate patient-specific MC-based dose maps associated with whole-body (WB) CT examinations in real-time using deep neural network algorithms. By using this dose map generation methodology and the organ segmentation part of our project described in 1.2.1 personalized CT dosimetry may be an alternative in the clinical routine.

2. Methodology

2.1 Application of AI in computational phantom generation through segmentation

Patient population

This part of our study included 2000 CT images (410,398 axial 2D slices) collected from multiple online available datasets (43, 44, 45, 46, 47, 48). The dataset contains both paediatric cases with 18.9 ± 4.13 cm Eq_diameter and adult cases with 27.53 ± 5.35 cm Eq_diameter as defined by AAPM #204 report. The masks (segmentations) for different 19 organs were used to train 19 different segmentation models. These CT images were acquired for a wide range of oncological indications and other applications, both with and without contrast enhancement.

Pre-processing

The body contour was extracted from the axial CT images through image processing algorithms which were used in former studies (49, 50). The CT images were cropped to a bounding box (BB) including the body contour in lateral and AP directions. The images were normalized before feeding them to the deep learning model.

---

[1] https://impactdose.software.informer.com/

Network architecture

A Res-UNET segmentation architecture was used. The modified version of U2Net (51, 52) was used in this study containing residual blocks. The input to the model was normalized and cropped CT images and the segmentation masks. **Figure 2** shows the network layers we have used in this part of study.
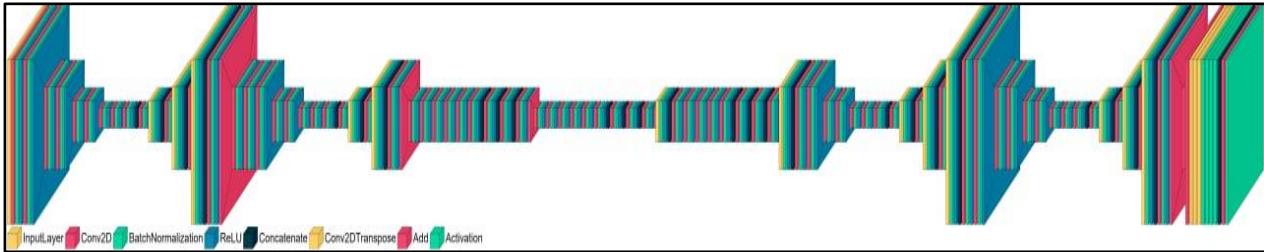

Figure 2. Architecture of the neural network we used for segmentation.

Evaluation metrics

For each organ segmentation task, 20 percent of each database was separated randomly and used as the test dataset. The predicted segmentations masks were compared to the ground truth masks by measuring Dice, Jaccard value, precision, and recall.

2.2 Applications of AI in internal dosimetry

2.1.1 Internal personalized dosimetry – ^{18}FDG-PET study

Study population

To provide whole-body dose maps from an activity map based on Eq. 1, a specific S-value kernel is required for each single voxel of the activity map. Whole-body unenhanced CT images of 24 patients acquired on Siemens Definition Edge system were used for the training of the model (generation of the training dataset). The study protocol was approved by the institution Ethics committee. For evaluation of the model, hybrid PET/CT image sets consisting of a low-dose CT scan and dynamic whole-body PET scans were employed. The hybrid PET/CT image sets were acquired on a Siemens Biograph mCT scanner using a dynamic scanning protocol at 13-time points after intravenous injection of ^{18}F-FDG (53, 54). PET scanning was conducted using continuous bed motion scan at ever increasing time intervals. PET image reconstruction was performed using 3D iterative ordinary Poisson OSEM (3D-OP-OSEM) algorithm with a voxel size of $4.07 \times 4.07 \times 3$ mm.

Data preparation and Monte Carlo simulation

To prepare the training data set, density maps were extracted from CT images. We converted HU values to mass density using the methodology proposed by Schneider *et al.* Based on linear multi-regression models (55). We extracted density maps consisting of 13 tissue densities, including air, lung, fat, soft tissue, and bone where values higher than 100 HUs were divided into eight discrete density values. Afterward, the whole-body density maps were resampled to 3 mm voxel size in three-dimensions. To build the ground truth data, MC simulations served as standard of reference. The MCNP transport code (56) was employed for the generation of energy deposition kernels, i.e. specific voxel S-values. To this end, one voxel was randomly sampled from the whole-body density maps and a 3D matrix of 64×64×64 voxels around the central voxel was extracted. This matrix, representing a heterogeneous medium of patients' anatomical structures, was directly imported to the MCNP code. The central voxels of the extracted 3D matrix were defined as source location with uniform distribution of Fluorodeoxyglucose (^{18}F-FDG). Since the resolution of the activity distribution (here PET images with an average resolution of 3 mm) determines the spatial accuracy of dosimetry estimations, we adopted the same resolution for the calculation of dose maps. The energy spectrum of emitted positrons was taken from (57), where the positron energy spectrum follows a Fermi distribution with an average of 242.8 KeV and maximum energy of 633.5 KeV. The output of MC simulations consist of 3D kernels (64×64×64) with 3 mm resolution using energy deposition mesh tally in unit of MeV/cm^3 per particle. Three million

particles were tracked to reach a statistical uncertainty less than 4% in the border voxels at about 10 cm away from the central voxel.

Deep neural network architecture

In this work, the *ResNET* (58) architecture implemented on TensorFlow platform, composed of 20 convolutional layers with dilation convolution operations within different levels of feature extraction, was utilized. For the training of the model, pairs of CT density images and deposited energy kernels were considered as input/target, respectively. The *ResNET* model with a 3D spatial window equal to 3×3×3 voxels were used. The following setting was used for the training of the network: learning rate = 0.001, sample per volume = 1, optimizer = Adam, and decay = 0.0001. The optimization of the network was carried out based on the L2 loss function.

Whole-body dose map calculation

To estimate whole-body voxelwise absorbed dose, the trained model was fed with patient-specific density maps to generate the specific dose distribution kernels, $S(voxel_k \leftarrow voxel_h)$, for each single voxel (i.e. $voxel_k$) in the PET image. The predicted specific S-values were corrected by element-wise multiplication of the ratio of the energy-absorption coefficient of the target voxel to the source voxel obtained from (59). Lastly, specific S-values underwent voxelwise convolution with the cumulated activity map to create the whole-body dose map. The cumulated activity map was calculated by analytical integration of voxelwise time activity curves over 13-time points dynamic PET frames.

Quantitative analysis

To evaluate the proposed method, the predicted absorbed dose from the current model was compared against direct MC dose estimation serving as standard of reference and different MIRD-based approaches, including the OLINDA/EXM software (organ-scale MIRD formalism) (60), single voxel S-value (SSV) and multiple voxel S-value (MSV) (61). For organ-level dosimetry, regions-of-interest were manually drawn on CT images to delineate eight organs, namely brain, heart, kidneys, liver, lungs, spleen, bone, and bladder. Lesions identified on PET images were segmented using a fixed threshold of 42% of SUV_{max} and manually edited to remove the background and include necrotic regions. The kinetic data required by Olinda/EXM software were calculated from the cumulated activity and the masses of organs were modified based on organ masks defined from the segmentation of CT images. SSV and MSV voxel-scale dosimetry was designed based on the MIRD formalism where the voxel S-value kernels were generated from MCNP code with the same kernel size used in the previous step. Ten million particles were simulated to build a 64×64×64 kernel in an infinite homogenous medium considering a unit activity in the central voxel. In the MSV method (62), the S-value kernels of four different media consisting of soft-tissue, lung, and two different densities of bone (with different Calcium content) were simulated. Voxelwise mean absolute error (MAE), mean relative absolute error (MRAE %), and root mean square error (RMSE) were calculated between reference and predicted dose maps.

2.1.2 Internal personalized dosimetry - Lu177 study

We extended our model on ^{18}F-FDG to a betta-emitter therapeutic agent, 177Lu-DOTATAE, using transfer learning that outperformed conventional methods, such as local energy deposition and MIRD formalism in high density regions (i.e. bone metastasis). This study using clinical data is under preparation.

2.3 Applications of AI in CT external beam dosimetry

Study population

This part of our project included 63 patients (35 male and 28 females) who underwent whole-body PET/CT imaging on a Biograph mCT scanner (Siemens Healthineers, Erlangen, Germany). All CT scans were performed in helical mode using 120 kVp tube potential, and Siemens CareDose4D TCM was activated. Images were reconstructed with the extended 70 cm field-of-view option, voxel size equal to 1.523 mm in the

axial plane, and 1.4 mm slice thickness using filtered-back projection algorithm. Figure 3 shows the flowchart of the different steps followed in this study protocol.
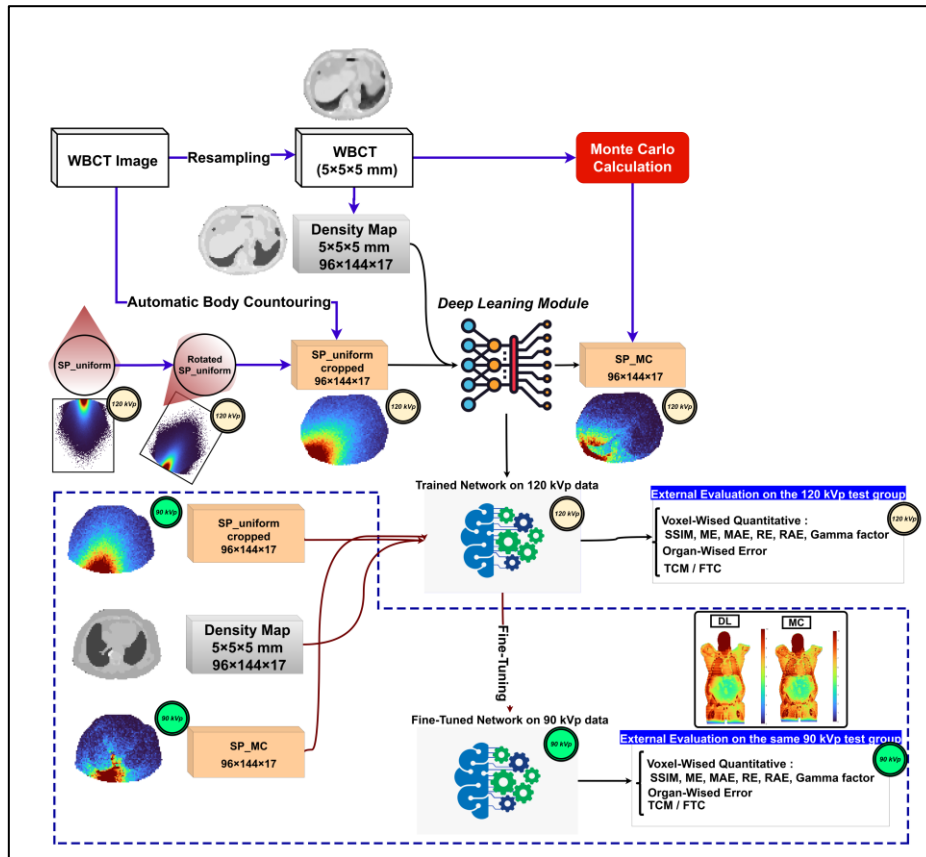
Figure 3. Flowchart summarizing the different steps involved in the implementation of the whole process. The blue dashed line shows the 90 kVp generalizability test. DL: Deep learning. MC: Monte Carlo.

Monte Carlo simulations

CT HU values were converted to density maps using linear multi-regression models for the segmentation of CT images into different tissue densities, as proposed by Schneider et al. (63). Subsequently, the resulting density maps were resampled to 5 mm³ cubic isotropic voxel size. The essential components incorporated into MC simulations, including accurate source model and protocol-related parameters, were adopted from our in-house MC simulation code developed and validated in a previous study (64). The acquisition parameters, including tube voltage, collimation width, table speed, rotation time, pitch, and tube current modulation, were implemented in this simulation. This simulator is based on the MCNPX general-purpose Monte Carlo radiation transport code (version 2.6) (65).

The output of MC simulations is a 3D dose map for a single source position (SP_MC) with limited axial coverage. Monte Carlo simulations were run for multiple discrete source positions to simulate helical whole-body CT scanning. A random starting location was generated for the source owing to the lack of information about the tube start angle in the DICOM header. Accordingly, a spiral motion of the source position in 2 mm axial intervals along the Z-axis (craniocaudal axis) was modeled. Finally, considering the longitudinal tube current modulation (extracted from the DICOM header for TCM), simulated dose maps for each source position was multiplied by the corresponding tube current and were superimposed to construct the complete voxel dose distribution.

Data preparation

MC calculations were performed for a total number of 63 patients with 120 kVp tube voltage. Then, by keeping all parameters similar, except kVp, MC calculations were repeated with 90 kVp tube voltage for patients in

the test group (11 cases) plus 20 cases randomly selected from the train and validation groups to perform the fine-tuning process described later in the text. The cases from the train and validation were used for performing transfer learning and fine-tuning.

Monte Carlo calculation of radiation dose in a uniform cylinder at 90 and 120 kVp

A uniform water-filled cylinder with a 715 mm diameter located within the CT gantry was simulated, and the dose map for a single source position (zero degrees, located at the anterior point) was calculated for a large number of simulated events (4×10^{10} particles) tracked by the MC simulator. This dose map, referred to as the single-source position uniform map (SP_uniform), was calculated for two tube voltages, namely 90 and 120 kVp for a single source. It should be mentioned that the 90 kVp uniform dose maps were used for testing the network generalizability through fine-tuning.

Generation of single-source position images and corresponding density maps

The body contour was automatically segmented on all CT images utilizing analytical image processing methods. All body contour segmentations were reviewed and confirmed visually. The MC output images (SP_MC) having a size of 96×144×17 voxels were saved, and the density map for the same axial coverage range cropped to the same size. The SP_uniform images were cropped to the same axial coverage body contour and normalized to a conversion factor (CF) calculated by Eq. (1) to compensate for the effect of attenuation taking place in the SP_uniform dose calculation on the large cylinder. The SP-uniform dose image calculated for the source at zero-degree position (patient's anterior in supine position) was rotated to match the desired angle (rotated SP_uniform in **Figure 3**)

$$\mathrm{CF} = e^{\left(d_{SP\_MC} - d_{SP\_uniform}\right)}. \qquad \text{Eq. (1)}$$

where e is Euler's number, d_{SP_MC} is the distance from the edge of the body contour to the x-ray tube source in a specific source position. $d_{SP\_uniform}$ is the distance from the edge of a large cylinder simulated to the source in a specific position. Since the cylinder size was larger than the size of our largest patient, the CF was always greater than 1.

SP_uniform and SP_MC images were normalized by all voxel intensities by a fixed value. Each source position was saved in a separate image and used for training the neural network.

Network architecture and training details

From all 63 WB CT images (27,632 source positions), 11 cases (4792 source positions) were used as the untouched test set. **Figure 3** shows the steps performed in this study and examples of mentioned three images of SP_uniform, SP_MC and density maps. The SP_unifrom in a unique source position/angle and the density map images were fed as input to the neural network to predict the SP_MC image as the output in the corresponding source position/angle. A deep residual network (ResNet) was trained in Python (TensorFlow) to generate the SP_MC images from the two mentioned inputs. The ResNet is composed of 20 convolutional layers (19 layers with kernel size 3×3×3 and the last layer with kernel size 1×1×1) where the image size is kept constant through the different layers (no down or up pooling was applied). Different feature levels, including low, medium, and high, were extracted by using dilation of 0 (first seven layers), 2 (six middle layers) and 4 (six last layers), respectively, in a convolutional kernel. Every two layers were connected using a residual connection to avoid gradient vanishing or exploding. The training was continued for 100 epochs using the "Adam" optimizer and L2 loss function. The initial learning rate of 10^{-3} was reduced in a piecewise method every five epochs. The trained network was tested on the external group datasets, and the deep neural network output was named SP_DL.

Generalizability evaluation on 90 kVp data (Fine-tuning)

To test the generalizability of the proposed model for kVps other than 120 kVp, we performed MC simulations to calculate the voxel dose maps by considering the 90 kVp spectrum on the untouched test group (11 cases) and 20 patients selected from the train and validation group. The same pre-processing steps mentioned earlier

were followed to derive SP_MC, SP_uniform, and density maps at 90 kVp. The model trained on 120 kVp dataset was stored. This model with the trained weight and biases were used to initialize the new training (fine-tuning) process through transfer learning. The fine-tuning process was continued for 50 epochs with 1e-7 learning rate and the weights and biases were updated according to 90 kVp datasets with SP_unifrom and density maps as input and SP_MC image as output to the model. SP_uniform and density maps were fed to the fine-tuned network on 90 kVp training datasets, and SP_DL images at 90 kVp were generated for the same test group (11 cases). These SP_DL images were compared to SP_MC images at 90 kVp.

Dose map reconstruction from single source positions

The dose maps from the single source position were corrected by factors related to the tube calibration described in a previous study (64). The tube current was extracted from the DICOM header. Then, the dose maps corresponding to a single source position/angle were superimposed to reconstruct the whole-body dose maps (WBDM) using both SP_MC and SP_DL dose maps, referred to as WBDM_MC and WBDM_DL, respectively. The final WBDM was a matrix of $96 \times 144 \times Z$ voxels, where Z is the image size along the Z-axis, and the voxel value is the absorbed dose in that voxel in units of milli-gray (mGy). We have considered two strategies for WBDM calculation, fixed 100mA tube current (FTC) and TCM activated according to the actual tube current recorded from the DICOM images.

Evaluation metrics

Voxel-wise quantitative dose evaluation

The WBDM_DL images were compared with WBDM_MC images serving as the standard of reference (ground truth) at the voxel level. Voxel-wise parameters, including structural similarity index (SSIM), peak signal to noise ratio (PSNR) mean error (ME, mGy), mean absolute error (MAE, mGy), relative error (RE, %), relative absolute error (RAE, %), and gamma pass rate were calculated. Gamma pass rate, as described earlier by Low *et al.* (66) with 1 mm and 1% criterion, was considered.

Organ-level dose evaluation

In addition to voxel-wise errors, eight organs, including the Liver, Heart, Bones, Kidneys (both), Spleen, Bladder, Lungs (both), and brain, were segmented manually on the test WBCT images. The organ doses were estimated by calculating the mean voxel value on WBDM images inside the organ segmentations. The organ absorbed doses calculated on WBDM_DL and WBDM_MC were compared for each organ in terms of mean error (ME, mGy), mean absolute error (MAE, mGy), relative error (RE, %), and relative absolute error (RAE, %). These voxel-wise and organ-wised metrics were calculated for both 90 kVp and 120 kVp external datasets, considering both FTC and TCM scenarios.

Statistical analysis

The Kolmogorov-Smirnov test was used to check the normality of distributions. The mentioned organ-wise evaluation metrics were compared between the two groups of 90 and 120 kVps using the Mann-Whitney test. P-values less than 0.05 were considered statistically significant.

3. Results

3.1 Organ segmentation study

Table 1. Results of the performance of our segmentation models for different 19 organs included in this part of our role in Sinfonia project.

Organ Name	Dice	Jaccard	Precision	recall
Liver	96.94 ± 1.67	94.11 ± 3.01	95.1 ± 5.41	97.99 ± 3.21
Cardiac	91.6 ± 6.52	85.09 ± 9.82	83.46 ± 15.47	89.44 ± 11.49
Pancreas	77.53 ± 16.01	65.78 ± 19.18	86.46 ± 14.4	89.22 ± 15.4

Bones	94.16 ± 4.86	89.31 ± 7.81	97.27 ± 4.39	98.86 ± 2.26
Kidneys	94.06 ± 4.8	89.13 ± 7.59	93.42 ± 8.3	97.13 ± 4.65
Spleen	94.32 ± 9.89	90.33 ± 11.82	92.46 ± 14.43	98.24 ± 9.1
Bladder	83.42 ± 18	74.77 ± 21.25	83.32 ± 20.77	90.37 ± 16.46
Esophagous	73.22 ± 10.96	58.8 ± 12.33	91.33 ± 9.76	92.81 ± 9.58
Femural Heads	95.68 ± 2.8	91.84 ± 4.8	98.55 ± 3.56	99.17 ± 2.75
Spinal Cord	89.76 ± 3.64	81.61 ± 5.62	98.98 ± 4.14	99.74 ± 1.04
Aorta	93.03 ± 2.84	87.09 ± 4.75	97.05 ± 6.75	99.71 ± 1
Gall Bladder	77.13 ± 20.17	66.21 ± 21.64	84.14 ± 21.11	91.11 ± 18.25
IVC	80.6 ± 11.32	68.83 ± 14.37	90.49 ± 9.54	93.43 ± 8.12
Large Intestine	70.62 ± 11.97	55.78 ± 13.2	55.67 ± 12.64	82.48 ± 10.94
Portal Vein	60.78 ± 11.07	44.37 ± 10.73	75.61 ± 12.87	85.62 ± 11.13
Rectum	76.35 ± 16.07	63.85 ± 16.82	67.68 ± 20.26	85.6 ± 14.74
Stomach	85.4 ± 13.67	76.4 ± 16.18	79.2 ± 18.9	91.63 ± 13.34
Thymus	64.22 ± 23.51	51 ± 22.65	81.45 ± 21.34	84.82 ± 22.82
GI	88.89 ± 8.87	80.93 ± 11.79	80.61 ± 13	83.36 ± 8.11

The average Dice value is summarized in Table 1. The best dice values were for lung and liver and the worse dice values were for thymus and large intestine. Figure 4 shows examples of 3D rendered segmentation in the test group visualized by colours. Figure 5 shows the distribution of the Dice coefficient in boxplots for different organs. Table 1 summarizes the Dice coefficients, Jaccard coefficients, precision, and recall on the external evaluation datasets.
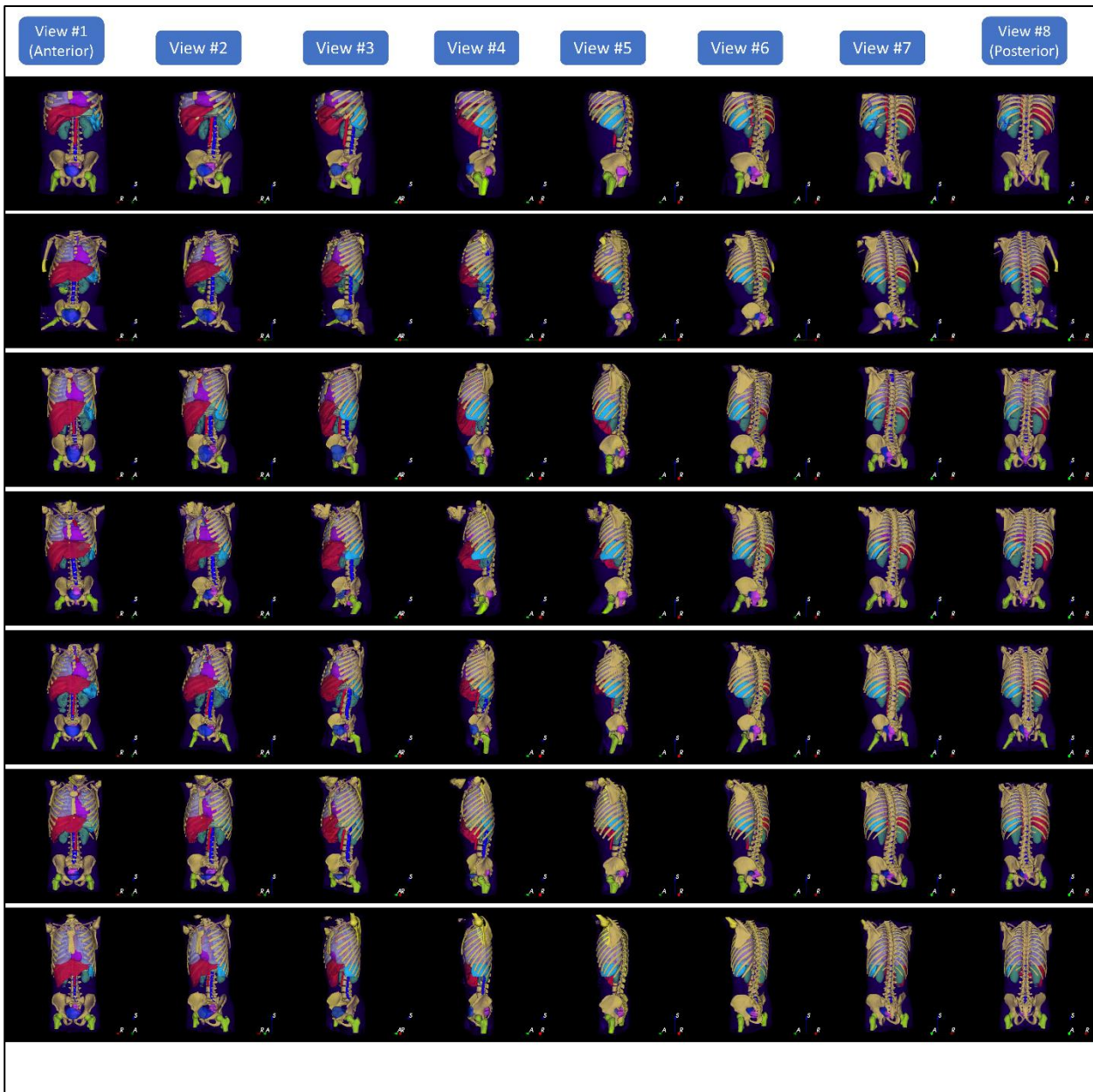
Figure 4. 3D rendered visualization of the segmentation masks generated on the external datasets.
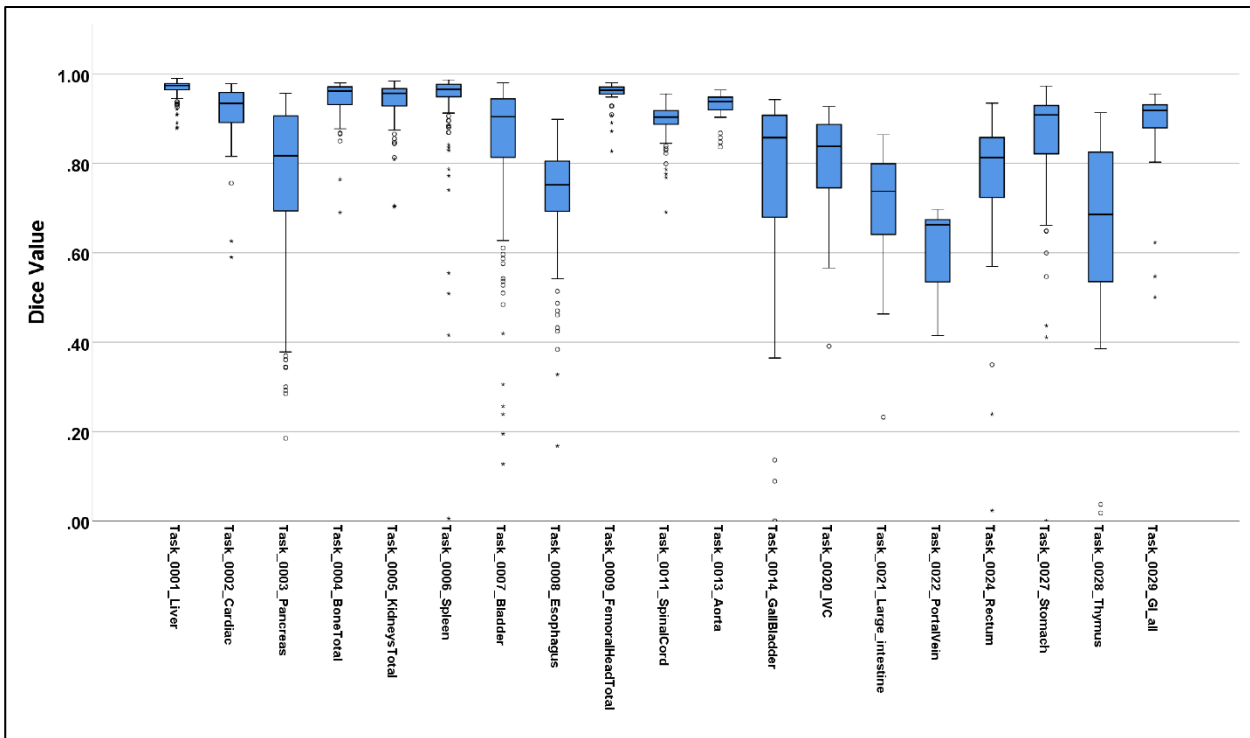
Figure 5. Boxplots of Dice coefficients for each segmented organ.

Among the limitations of this study is that there are lot of organs which are not easily recognizable on CT images, especially small organs with low contrast on CT images. This is an inherent limitation of organ segmentation from CT images, which impacts DL segmentation performance. As such, a number of organs are missing, which precludes calculation of effective doses from CT examinations.

3.2.1 ^{18}FDG-PET study

The model performance in terms of quantitative comparison of voxel-wise predicted dose with respect to the MC ground truth is illustrated in *Figure 6*. The specific voxel-wise S-value kernels, obtained from the deep neural network (DNN), showed a good agreement with the results obtained from the reference MC kernels with MRAE, RMSE, and MAE of 4.5±1.8 (%), (1.8 ± 0.53) ×10-5 (MeV/cm^3) and (1.8±0.71)×10^{-6} (MeV/cm3), respectively.
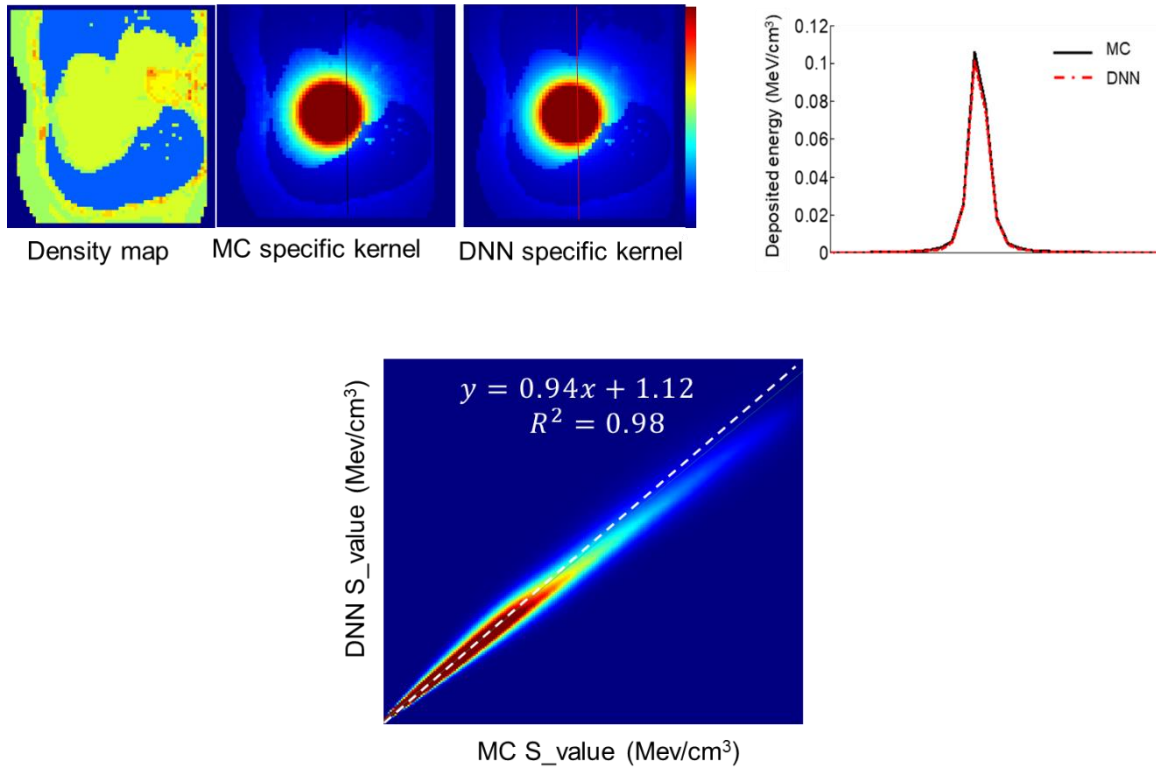
Figure 6. (a) CT-based density map, (b) reference kernel obtained from MC simulations, (c) predicted kernel by the DNN model. Line profiles across the S-value kernels (right panel) comparing kernels obtained from MC simulations of DNN model predictions. Voxelwise joint histogram plot depicting the correlation of predicted kernels with respect to MC simulations.

Whole-body voxel-wise dose maps predicted by DNN, MSV, and SSV were compared to that obtained from the MC simulation where MRAEs of 2.6%, 3%, and 49% were obtained, respectively (Figure 7).
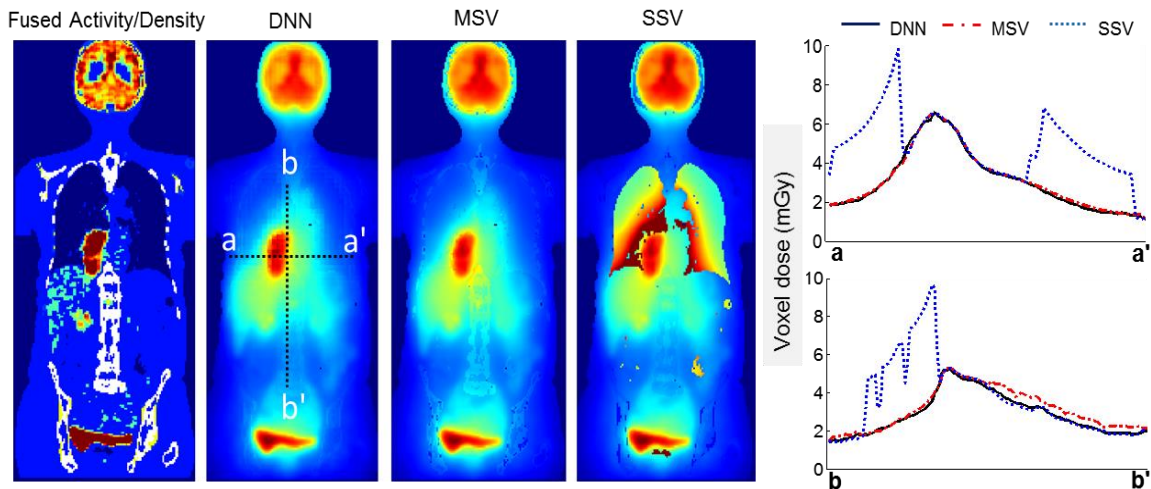
Figure 7. Voxel-wise dose maps estimated using DNN, MSV, and SSV along with horizontal and vertical profiles drawn on the coronal view.

Organ-level dosimetry has been extracted from the dose maps for the different methods and compared against a commercial organ-based MIRD dosimetry software, i.e. Olinda/EXM (**Figure 8**). The MARE between absorbed doses in different organs estimated by the DNN method compared to MSV, SSV, and Olinda were 5.1%, 21.8%, and 23.5%, respectively.
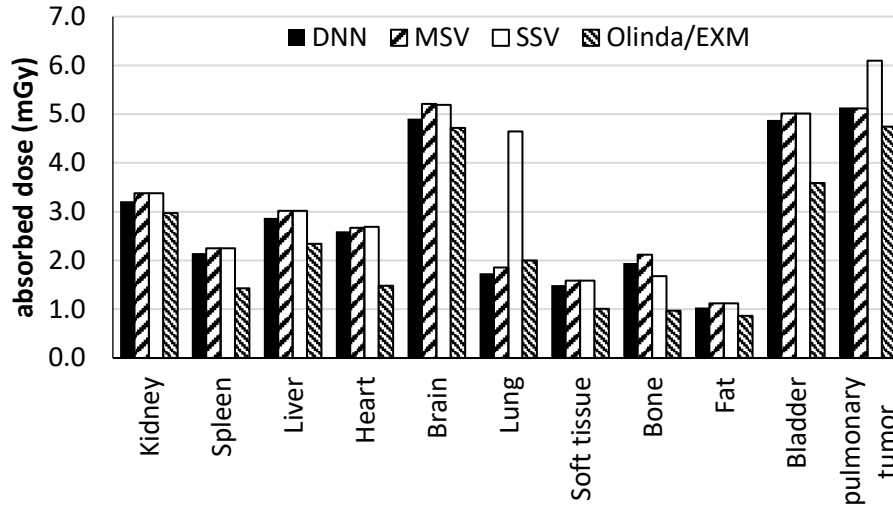
Figure 8. Whole-body organ-level absorbed doses estimated using DNN, MSV, SSV and Olinda/EXM software.

Among the limitations of this study is the low number of cases (sample size), owing to time-consuming Monte-Carlo calculations required to generate the standard of reference.

3.3 Deep dose CT study

Patients' demographics

The age of included patients was 58.9 ± 17.2 years. The average patients' water equivalent diameter was 26.6±2.7 (range 16.45 - 32.95) cm. The average tube current implemented by TCM was 140.7 ±48.71 (56 to 306) mA. **Table 2** summarizes the demographic information of patients.

Table 2. Demographic description of the test and train & validation groups.

metric	Train & Validation	Test
sex	29 male, 23 female	6 male, 5 female
age	60.1 ± 16.9	53.2 ± 17.9
kVp	120	120
Pitch	0.8	0.8
CTDIvol	5.74±2.70	8.33 ± 4.00
Patient Height	169 ± 12	167 ± 12
Patient Weight	75.1 ± 15.8	76.4 ± 17.4
Tube Current	135.5 ± 45.4	167.6 ± 67.8

Voxel-wise error metrics

Table 3 summarizes the results of voxel-wise metrics for two external validation groups acquired at 90 and 120 kVp. The model performance for the 120 kVp and TCM test set in terms of voxel-wise parameters, including SSIM, PSNR, Gamma pass rate, ME, MAE, RE, and RAE, was 0.997 ± 0.002, 46.69 ± 1.98, 98.47 ± 0.81, -0.0359 ± 0.0244 mGy, 0.1091 ± 0.0279 mGy, -1.16 ± 1.41 %, and 7.13 ± 0.44 %, respectively. All voxel-wise parameters were in the same range for 120 kVp, TCM and FTC test sets. The voxel-wise evaluation results after performing transfer learning and fine-tuning on 90 kVp data were also comparable to 120 kVp, except RAE, which was almost 1.5% higher in the 90 kVp test group compared with 120 kVp results (8.63 vs. 7.17). Considering the FTC and TCM scenarios, the performance of our model was almost similar in the 90 kVp test set.

Figure 9 shows the joint histogram comparing WBDM_DL and WBDM_MC doses at the voxel level. The high correlation depicted in **Figure 9** (R2>0.98) and other voxel-wise metrics show excellent agreement between MC and DL dose maps.
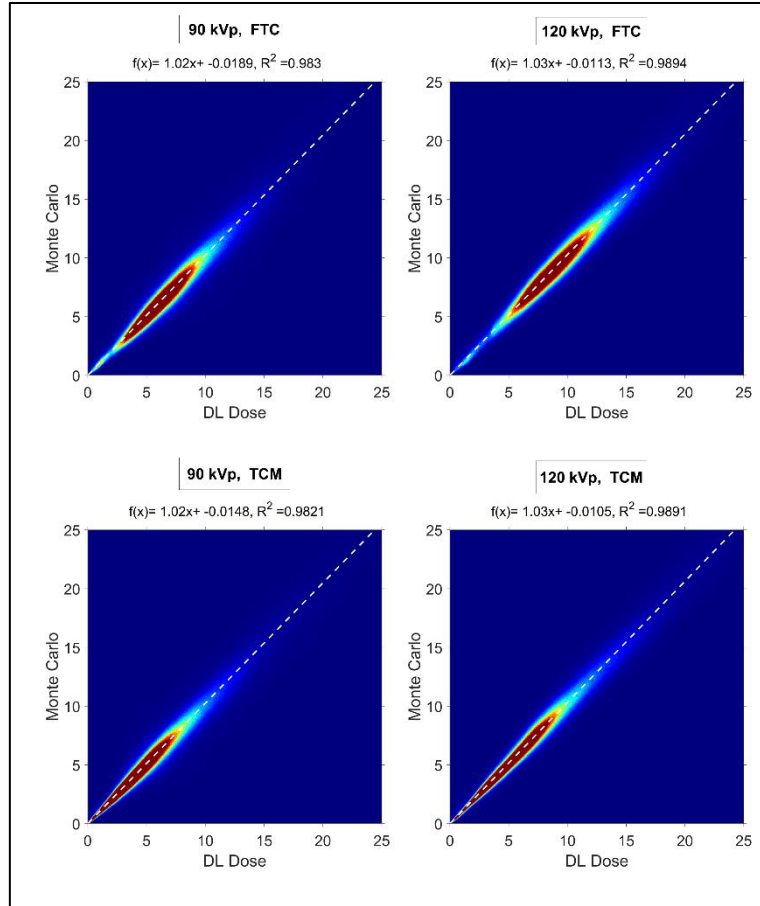
Figure 9. Joint histogram comparing DL and MC dose maps at the voxel level.

Figure 10 shows two examples of WBDM_DL and WBDM_MC and their corresponding bias maps displayed in a coronal view for a combination of two kVps (90 and 120) and two TCM and FTC scenarios. The bias map shows excellent agreement between MC and DL results. The highest differences in terms of RAE (%) are depicted in the lung/chest wall interval and soft tissue/skull (bony tissue), where there is a gradient in density and chemical composition characteristics of biological tissues and, consequently, radiation interaction properties with tissues. The average RAE for all organs was always less than 4.5 % for both kVps and TCM and FTC scenarios.
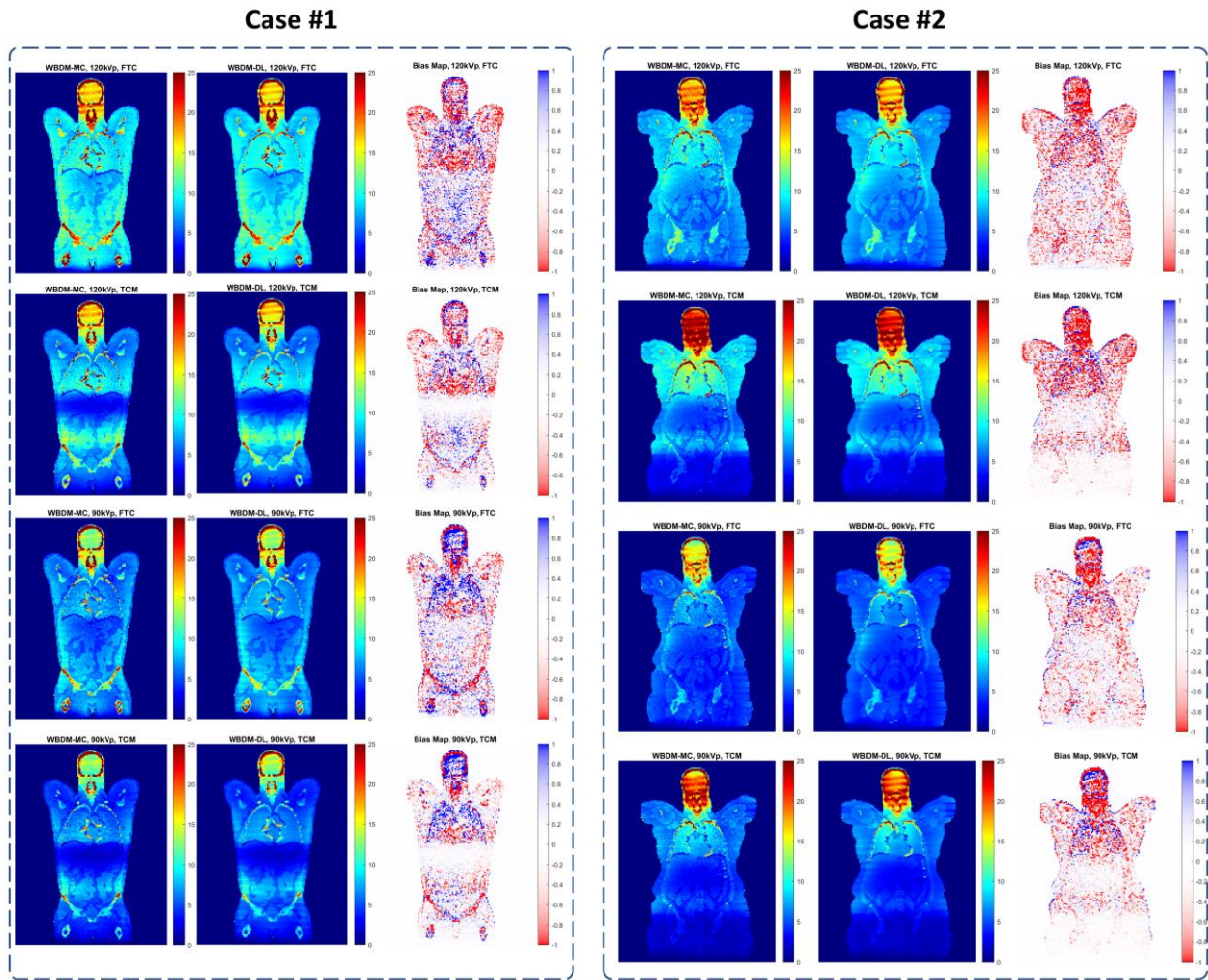
Figure 10. Coronal slices of WBDM_DL, WBDM_MC and the corresponding bias maps for two cases from the external test sets. The caption for each study displays the kVp and tube current scenario (TCM or FTC). Case #1: 74 y/o male, patient height = 172 cm, patient weight = 85 kg, average water equivalent diameter (46) = 28.4 cm, the effective diameter at the largest slice = 32.9 cm. case #2: 65 y/o female, patient height = 158 cm, patient weight = 87 kg, water equivalent diameter = 29.5 cm, the effective diameter at the largest slice = 35.6 cm. The voxel value here is mGy, and the color bar is shown beside each image

Table 3. Summary of voxel-wised metrics calculations.

	120 kVp		90 kVp	
	FTC	**TCM**	**FTC**	**TCM**
SSIM	0.997 ± 0.002 (0.993 to 0.998)	0.997 ± 0.002 (0.993 to 0.998)	0.994 ± 0.005 (0.981 to 0.998)	0.994 ± 0.005 (0.981 to 0.998)
PSNR	46.69 ± 1.98 (44.95 to 50.17)	47.68 ± 1.98 (44.95 to 50.17)	45.11 ± 3.85 (37.51 to 48.77)	46.18 ±5.08 (37.48 to 51.66)
Gamma Value	98.47 ± 0.81 (96.73 to 99.72)	98.91 ±0.81 (96.73 to 99.72)	98.26 ± 1.29 (95.28 to 99.08)	98.64 ± 1.41 (95.28 to 99.68)
ME (mGy)	-0.0359 ± 0.0244 (-0.0826 to 0.0025)	-0.0302 ± 0.0244 (-0.0826 to 0.0025)	-0.0167 ± 0.0149 (-0.0372 to 0.0161)	-0.0126 ± 0.0124 (0.0326 to 0.0133)
MAE (mGy)	0.1091 ± 0.0279 (0.0513 to 0.1401)	0.0854 ± 0.0279 (0.0513 to 0.1401)	0.1088 ± 0.0308 (0.0776 to 0.1626)	0.0892 ± 0.0462 (0.0471 to 0.1713)
RE (%)	-1.16 ± 1.41 (-3.72 to 1.39)	-1.13 ± 1.41 (-3.72 to 1.39)	0.27 ± 1.33 (-1.99 to 2.00)	0.28 ± 1.33 (-2.00 to 1.98)
RAE (%)	7.13 ± 0.44 (6.57 to 7.89)	7.17 ± 0.44 (6.57 to 7.89)	8.58 ± 1.83 (6.15 to 10.80)	8.63 ± 1.82 (6.19 to 10.82)

Table 4. Results of organ-wise evaluation of the results for the 120 kVp dataset.

	Organ	FTC				TCM			
		RE %	RAE %	ME (mGy)	MAE (mGy)	RE %	RAE %	ME (mGy)	MAE (mGy)
120 kVp	Liver	-0.27 ± 1.54 (-2 to 3.32)	1.26 ± 0.84 (0.42 to 3.32)	-0.023 ± 0.158 (-0.244 to 0.32)	0.128 ± 0.086 (0.055 to 0.32)	-0.27 ± 1.54 (-2 to 3.32)	1.26 ± 0.84 (0.42 to 3.32)	-0.023 ± 0.158 (-0.244 to 0.32)	0.128 ± 0.086 (0.055 to 0.32)
	Heart	-3.09 ± 1.77 (-6.02 to 0.36)	3.16 ± 1.63 (0.36 to 6.02)	-0.331 ± 0.19 (-0.658 to 0.041)	0.338 ± 0.175 (0.041 to 0.658)	-3.09 ± 1.77 (-6.02 to 0.36)	3.16 ± 1.63 (0.36 to 6.02)	-0.331 ± 0.19 (-0.658 to 0.041)	0.338 ± 0.175 (0.041 to 0.658)
	Bone	-1.31 ± 1.98 (-4.58 to 2.9)	1.86 ± 1.41 (0.12 to 4.58)	-0.146 ± 0.24 (-0.482 to 0.427)	0.227 ± 0.156 (0.017 to 0.482)	-1.31 ± 1.98 (-4.58 to 2.9)	1.86 ± 1.41 (0.12 to 4.58)	-0.146 ± 0.24 (-0.482 to 0.427)	0.227 ± 0.156 (0.017 to 0.482)
	Kidneys	-0.56 ± 1.88 (-5.31 to 1.37)	1.2 ± 1.51 (0.07 to 5.31)	-0.037 ± 0.132 (-0.284 to 0.109)	0.097 ± 0.093 (0.005 to 0.284)	-0.56 ± 1.88 (-5.31 to 1.37)	1.2 ± 1.51 (0.07 to 5.31)	-0.037 ± 0.132 (-0.284 to 0.109)	0.097 ± 0.093 (0.005 to 0.284)
	Spleen	-0.05 ± 2.3 (-5.15 to 3.85)	1.6 ± 1.57 (0.11 to 5.15)	0.011 ± 0.188 (-0.337 to 0.356)	0.138 ± 0.12 (0.009 to 0.356)	-0.05 ± 2.3 (-5.15 to 3.85)	1.6 ± 1.57 (0.11 to 5.15)	0.011 ± 0.188 (-0.337 to 0.356)	0.138 ± 0.12 (0.009 to 0.356)
	Bladder	2.39 ± 3.73 (-2.89 to 11.64)	3.11 ± 3.1 (0.48 to 11.64)	0.229 ± 0.328 (-0.221 to 1.05)	0.282 ± 0.28 (0.06 to 1.05)	2.39 ± 3.73 (-2.89 to 11.64)	3.11 ± 3.1 (0.48 to 11.64)	0.229 ± 0.328 (-0.221 to 1.05)	0.282 ± 0.28 (0.06 to 1.05)
	Lungs	-2.42 ± 1.3 (-4.34 to -0.45)	2.42 ± 1.3 (0.45 to 4.34)	-0.275 ± 0.135 (-0.473 to -0.046)	0.275 ± 0.135 (0.046 to 0.473)	-2.42 ± 1.3 (-4.34 to -0.45)	2.42 ± 1.3 (0.45 to 4.34)	-0.275 ± 0.135 (-0.473 to -0.046)	0.275 ± 0.135 (0.046 to 0.473)
	Brain	-3.52 ± 3.25 (-7.87 to 3.05)	4.15 ± 2.29 (0.43 to 7.87)	-0.587 ± 0.525 (-1.198 to 0.45)	0.681 ± 0.38 (0.066 to 1.198)	-3.52 ± 3.25 (-7.87 to 3.05)	4.15 ± 2.29 (0.43 to 7.87)	-0.587 ± 0.525 (-1.198 to 0.45)	0.681 ± 0.38 (0.066 to 1.198)
	All Organs	-1.10 ± 2.89 (-7.87 to 11.63)	2.34 ± 2.01 (0.07 to 11.63)	-0.144 ± 0.348 (-1.198 to 1.049)	0.270 ± 0.261 (0.005 to 1.198)	-1.11 ± 2.90 (-7.84 to 11.76)	2.34 ± 2.03 (0.08 to 11.76)	-0.144 ± 0.342 (-1.497 to 0.765)	0.23 ± 0.28 (0.01 to 1.49)

Table 5. Organ-wise evaluation of the results for the 90 kVp dataset after fine-tuning.

	Organ	FTC				TCM			
		RE %	RAE %	ME (mGy)	MAE (mGy)	RE %	RAE %	ME (mGy)	MAE (mGy)
90 kVp	Liver	-0.41 ± 1.83 (-3.3 to 3.76)	1.37 ± 1.22 (0.14 to 3.76)	-0.04 ± 0.155 (-0.305 to 0.299)	0.112 ± 0.109 (0.009 to 0.305)	-0.5 ± 1.81 (-3.15 to 3.78)	1.37 ± 1.22 (0.07 to 3.78)	-0.036 ± 0.114 (-0.262 to 0.211)	0.08 ± 0.085 (0.001 to 0.262)
	Heart	-3.81 ± 2.3 (-6.29 to 1.03)	4.01 ± 1.9 (0.04 to 6.29)	-0.325 ± 0.207 (-0.557 to 0.095)	0.343 ± 0.173 (0.002 to 0.557)	-3.85 ± 2.32 (-6.27 to 1.03)	4.04 ± 1.92 (0.04 to 6.27)	-0.24 ± 0.177 (-0.455 to 0.078)	0.255 ± 0.153 (0.002 to 0.455)
	Bone	-3.16 ± 2.72 (-5.72 to 4.15)	3.92 ± 1.22 (1.56 to 5.72)	-0.282 ± 0.255 (-0.463 to 0.433)	0.361 ± 0.097 (0.167 to 0.463)	-3.06 ± 2.75 (-5.72 to 4.2)	3.82 ± 1.34 (0.8 to 5.72)	-0.212 ± 0.223 (-0.491 to 0.353)	0.276 ± 0.124 (0.101 to 0.491)
	Kidneys	-1.81 ± 2.12 (-6.42 to 0.27)	1.86 ± 2.07 (0.2 to 6.42)	-0.101 ± 0.11 (-0.33 to 0.014)	0.104 ± 0.107 (0.01 to 0.33)	-2.03 ± 2.08 (-6.42 to 0)	2.03 ± 2.08 (0 to 6.42)	-0.078 ± 0.08 (-0.223 to 0)	0.078 ± 0.08 (0 to 0.223)
	Spleen	-1.33 ± 2.08 (-4.5 to 2.05)	1.99 ± 1.39 (0.16 to 4.5)	-0.085 ± 0.134 (-0.314 to 0.12)	0.127 ± 0.091 (0.007 to 0.314)	-1.25 ± 2.22 (-4.7 to 2.77)	1.96 ± 1.56 (0.05 to 4.7)	-0.056 ± 0.079 (-0.203 to 0.083)	0.075 ± 0.059 (0.001 to 0.203)
	Bladder	1.59 ± 4.3 (-3.66 to 11.86)	3.1 ± 3.27 (0.31 to 11.86)	0.109 ± 0.285 (-0.275 to 0.787)	0.211 ± 0.213 (0.013 to 0.787)	1.61 ± 4.22 (-3.57 to 11.74)	3.05 ± 3.23 (0.31 to 11.74)	0.067 ± 0.133 (-0.083 to 0.383)	0.101 ± 0.106 (0.013 to 0.383)
	Lungs	1.42 ± 2.5 (-2.35 to 6.59)	2.12 ± 1.88 (0.11 to 6.59)	0.112 ± 0.211 (-0.236 to 0.549)	0.178 ± 0.154 (0.008 to 0.549)	1.46 ± 2.43 (-2.25 to 6.4)	2.09 ± 1.86 (0.04 to 6.4)	0.096 ± 0.165 (-0.133 to 0.425)	0.14 ± 0.125 (0.002 to 0.425)
	Brain	2.19 ± 4.88 (-3.72 to 14.13)	3.57 ± 3.88 (0.06 to 14.13)	0.239 ± 0.56 (-0.522 to 1.528)	0.426 ± 0.421 (0.008 to 1.528)	2.11 ± 4.74 (-3.72 to 13.57)	3.5 ± 3.73 (0.15 to 13.57)	0.37 ± 0.884 (-0.522 to 2.702)	0.572 ± 0.756 (0.013 to 2.702)
	All Organs	-0.67 ± 3.59 (-6.42 to 14.13)	2.74 ± 2.40 (0.04 to 14.13)	-0.047 ± 0.321 (-0.557 to 1.528)	0.233 ± 0.224 (0.002 to 1.528)	-0.69 ± 3.57 (-6.42 to 13.57)	2.73 ± 2.38 (0.01 to 13.57)	-0.011 ± 0.375 (-0.522 to 2.702)	0.197 ± 0.318 (0.001 to 2.701)

Organ-wise error metrics

SINFONIA

D2.2 - Software tool on personalised dosimetry in PET-CT and deep learning-guided algorithms for automated construction of computational models
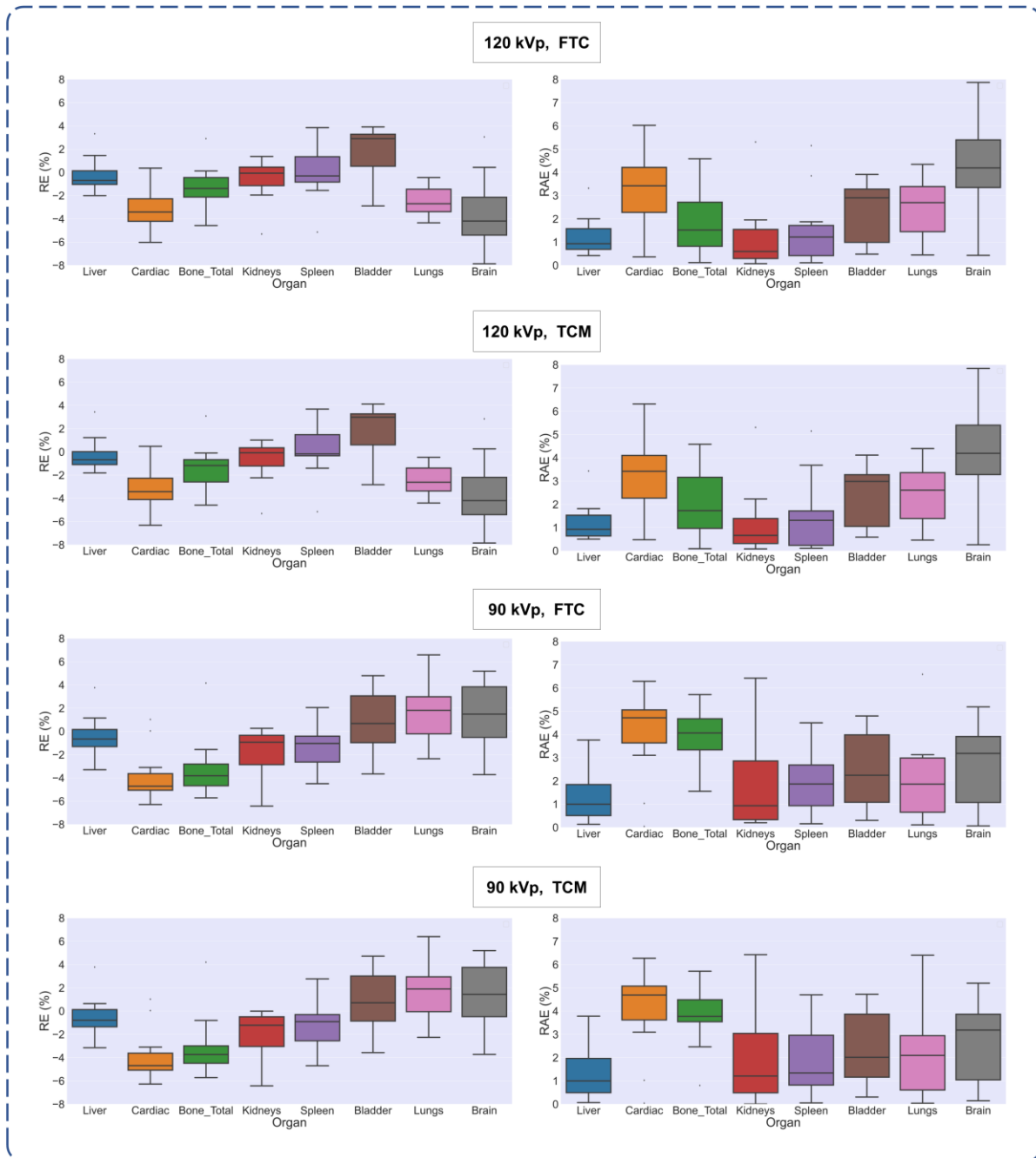

Figure 11. Boxplots of the RE and RAE (%) comparing organ doses calculated by DL and MC methods for eight segmented organs and a combination of 90 and 120 kVps and TCM/FTC scenarios.

The organ-wise error for 120 kVp and TCM scenario averaged over all segmented organs in terms of RE (%), RAE (%), ME (mGy), and MAE (mGy) was -1.11 ± 2.90, 2.34 ± 2.03, -0.144 ± 0.342, and 0.23 ± 0.28 respectively. ***Table 4*** and ***Table 5*** summarize organ-wise metrics calculated on 120 kVp and 90 kVp test sets, respectively. There was no statistically significant difference between the metrics calculated in organ-wise evaluations between the FTC and TCM performance in either the 90 and 120 kVp test sets (Mann-Whitney, p>>0.05). The highest average errors were observed in the heart, bones, and brain regions, where there is a higher gradient in density and surrounding tissues. The violin plots show overall excellent agreement between the distributions of DL and MC organ doses. Figure 11 shows the boxplot of RE and RAE (%) between the calculated organ doses.

It should be mentioned that the developed model is scanner-specific and, and as such, it requires fine-tuning for new scanners with different geometries and tube characteristics.

4. Conclusions

In this part of our contribution to Sinfonia project, we aimed to provide a methodology for fast and accurate personalized dosimetry in hybrid imaging protocols in nuclear medicine, such as SPECT/CT and PET/CT as well as radiation dosimetry in theragnostic applications of nuclear medicine. We attempted to address the problem in two steps for generating voxel radiation dose maps and organs segmentation. Our approach has shown good performance for both steps of dose map generation and organ segmentation in either internal or external radiation dosimetry with much better accuracy than the available pre-tabulated or simplified methods. We used state-of-the-art deep learning and image processing algorithms that can be easily implemented within few minutes.

5. Future plans in the scope of Sinfonia project

1. Develop a deep neural network to estimate organ radiation dose directly from the geometrical and structural information in CT images.
2. Improve the accuracy of OARs segmentation pipeline.
3. Develop a deep neural network solution to help dosimetry in Y90-SIRT for treatment of liver malignancies.

6. References

1. Ritt P. Recent Developments in SPECT/CT. Sem Nucl Med. 2022;52(3):276-85.
2. Aide N, Lasnon C, Desmonts C, Armstrong IS, Walker MD, McGowan DR. Advances in PET/CT Technology: An Update. Sem Nucl Med. 2022;52(3):286-301.
3. Shi F, Hu W, Wu J, Han M, Wang J, Zhang W, et al. Deep learning empowered volume delineation of whole-body organs-at-risk for accelerated radiotherapy. Nature communications. 2022;13(1):6566.
4. Tang Y, Huo Y, Xiong Y, Moon H, Assad A, Moyo T, et al. Improving splenomegaly segmentation by learning from heterogeneous multi-source labels. SPIE Medical Imaging: SPIE; 2019.
5. Yang Y, Tang Y, Gao R, Bao S, Huo Y, McKenna MT, et al. Validation and estimation of spleen volume via computer-assisted segmentation on clinically acquired CT scans. J Med Imaging (Bellingham). 2021;8(1):014004.
6. Lindgren Belal S, Sadik M, Kaboteh R, Enqvist O, Ulén J, Poulsen MH, et al. Deep learning for segmentation of 49 selected bones in CT scans: First step in automated PET/CT-based 3D quantification of skeletal metastases. European Journal of Radiology. 2019;113:89-95.
7. Bolch WE, Bouchet LG, Robertson JS, Wessels BW, Siegel JA, Howell RW, et al. MIRD pamphlet No. 17: the dosimetry of nonuniform activity distributions--radionuclide S values at the voxel level. Medical Internal Radiation Dose Committee. J Nucl Med. 1999;40(1):11s-36s.
8. Johnson PB, Whalen SR, Wayson M, Juneja B, Lee C, Bolch WE. Hybrid patient-dependent phantoms covering statistical distributions of body morphometry in the US adult and pediatric population. Proc IEEE. 2009;97(12):2060-75.
9. Akhavanallaf A, Xie T, Zaidi H. Development of a Library of Adult Computational Phantoms Based on Anthropometric Indexes. Ieee T Radiat Plasma. 2019;3(1):65-75.
10. Na YH, Zhang B, Zhang J, Caracappa PF, Xu XG. Deformable adult human phantoms for radiation protection dosimetry: anthropometric data representing size distributions of adult worker populations and software algorithms. Phys Med Biol. 2010;55(13):3789.
11. Xie T, Akhavanallaf A, Zaidi H. Construction of patient-specific computational models for organ dose estimation in radiological imaging. Med Phys. 2019;46(5):2403-11.
12. Xie T, Zaidi H. Estimation of the radiation dose in pregnancy: an automated patient-specific model using convolutional neural networks. Eur Radiol. 2019;29(12):6805-15.

13. Berger MJ. Distribution of absorbed dose around point sources of electrons and beta particles in water and other media. National Bureau of Standards, Washington, DC; 1971.

14. Kolbert KS, Sgouros G, Scott AM, Bronstein JE, Malane RA, Zhang J, et al. Implementation and evaluation of patient-specific three-dimensional internal dosimetry. J Nucl Med. 1997;38(2):301-8.

15. Giap HB, Macey DJ, Bayouth JE, Boyer AL. Validation of a dose-point kernel convolution technique for internal dosimetry. Phys Med Biol. 1995;40(3):365-81.

16. Zaidi H. Relevance of accurate Monte Carlo modeling in nuclear medical imaging. Med Phys. 1999;26(4):574-608.

17. Gardin I, Bouchet LG, Assie K, Caron J, Lisbona A, Ferrer L, et al. Voxeldoes: a computer program for 3-D dose calculation in therapeutic nuclear medicine. Cancer Biother Radiopharm. 2003;18(1):109-15.

18. Stabin MG, Madsen MT, Zaidi H. Personalized dosimetry is a must for appropriate molecular radiotherapy. Med Phys. 2019;46(11):4713-6.

19. Kalender WA. Dose in x-ray computed tomography. Phys Med Biol. 2014;59(3):R129-R50.

20. Salimi Y, Deevband MR, Ghafarian P, Ay MR. Uncertainties in effective dose estimation for CT transmission scan in total body PET-CT imaging with Auto mA3D tube current modulation. International Journal of Radiation Research. 2018;16(4):465-72.

21. Menzel HG, Clement C, DeLuca P. ICRP Publication 110. Realistic reference phantoms: an ICRP/ICRU joint effort. A report of adult reference computational phantoms. Annals of the ICRP. 2009;39(2):1-164.

22. Tsalafoutas IA, Hassan Kharita M, Al-Naemi H, Kalra MK. Radiation dose monitoring in computed tomography: Status, options and limitations. Phys Med. 2020;79:1-15.

23. Li X, Steigerwalt D, Rehani MM. T-shirt size as a classification for body habitus in computed tomography (CT) and development of size-based dose reference levels for different indications. European journal of radiology. 2022;151:110289.

24. Ria F, Fu W, Hoye J, Segars WP, Kapadia AJ, Samei E. Comparison of 12 surrogates to characterize CT radiation risk across a clinical population. Eur Radiol. 2021;31(9):7022-30.

25. Klein L, Liu C, Steidel J, Enzmann L, Knaup M, Sawall S, et al. Patient-specific radiation risk-based tube current modulation for diagnostic CT. Med Phys. 2022;49(7):4391-403.

26. Martin CJ, Barnard M. How much should we be concerned about cumulative effective doses in medical imaging? Journal of radiological protection : official journal of the Society for Radiological Protection. 2022;42(1).

27. Zewde N, Ria F, Rehani MM. Organ doses and cancer risk assessment in patients exposed to high doses from recurrent CT exams. European journal of radiology. 2022;149:110224.

28. Arellano RS, Yang K, Rehani MM. Analysis of patients receiving >/= 100 mSv during a computed tomography intervention. Eur Radiol. 2021;31(5):3065-70.

29. Bayer HealthCare. Radimetrics Enterprise Platform: Dose Management Solution.: Bayer HealthCare; [Available from: http://www.radiologysolutions.bayer.com/products/ct/dosemanagement/rep/. .

30. Akhavanallaf A, Fayad H, Salimi Y, Aly A, Kharita H, Al Naemi H, et al. An update on computational anthropomorphic anatomical models. Digit Health. 2022;8:20552076221111941.

31. Guberina N, Suntharalingam S, Nassenstein K, Forsting M, Theysohn J, Wetter A, et al. Verification of organ doses calculated by a dose monitoring software tool based on Monte Carlo Simulation in thoracic CT protocols. Acta Radiol. 2018;59(3):322-6.

32. Al-Senan R, Brown K, Erdman M, King S. The uncertainty of thyroid dose estimate in chest CT. Biomed Phys Eng Express. 2020;6(6).

33. Tahiri M, Mkimel M, Benameur Y, El Baydaoui R, Mesradi MR, El Rhazouani O. Organ Dose Estimation for Adult Chest CT Examination Using GATE Monte Carlo Simulation. Phys Part Nuclei Let. 2021;18(4):502-9.

34. Sharma S, Kapadia A, Fu W, Abadi E, Segars WP, Samei E. A real-time Monte Carlo tool for individualized dose estimations in clinical CT. Phys Med Biol. 2019;64(21):215020.

35. De Man B, Wu M, FitzGerald P, Kalra M, Yin Z. Dose reconstruction for real-time patient-specific dose estimation in CT. Med Phys. 2015;42(5):2740-51.

36. van der Velden BHM, Kuijf HJ, Gilhuijs KGA, Viergever MA. Explainable artificial intelligence (XAI) in deep learning-based medical image analysis. Med Image Anal. 2022;79:102470.

37. Fu Y, Lei Y, Wang T, Curran WJ, Liu T, Yang X. Deep learning in medical image registration: a review. Phys Med Biol. 2020;65(20):20TR01.

38. Fu Y, Lei Y, Wang T, Curran WJ, Liu T, Yang X. A review of deep learning based methods for medical image multi-organ segmentation. Phys Med. 2021;85:107-22.

39. Maier J, Klein L, Eulig E, Sawall S, Kachelriess M. Real-time estimation of patient-specific dose distributions for medical CT using the deep dose estimation. Med Phys. 2022;49(4):2259-69.

40. Tzanis E, Damilakis J. A novel methodology to train and deploy a machine learning model for personalized dose assessment in head CT. Eur Radiol. 2022;32(9):6418-26.

41. Kulathilake KASH, Abdullah NA, Sabri AQM, Lai KW. A review on deep learning approaches for low-dose Computed Tomography restoration. Complex Intell Syst. 2022:*in press*.

42. Salimi Y, Shiri I, Akhavanallaf A, Mansouri Z, Saberi Manesh A, Sanaat A, et al. Deep learning-based fully automated Z-axis coverage range definition from scout scans to eliminate overscanning in chest CT imaging. Insights Imaging. 2021;12(1):162.

43. Patrick Bilic1a PFCa, Eugene Vorontsov1e,1, Grzegorz Chlebusr, Hao, Chenm, Qi Doum, Chi-Wing Fum, Xiao Hanp, Pheng-Ann Hengm, Jrgen Hesserq, Samuel, Kadourye, Tomasz Kopczyskiv, Miao Leo, Chunming Lio, Xiaomeng Lim, Jana Lipkov´aa,, John Lowengrubn HM, Jan Hendrik Moltzr, Chris Pale,1, Marie Pirauda,, Xiaojuan Qim JQ, 1, Markus Rempflera, Karsten Rothq, Andrea Schenkr, Anjany, Sekuboyinaa PZ, Christian H¨ulsemeyera, Marcel Beetza, Florian Ettlingera, Felix, et al. The Liver Tumor Segmentation Benchmark (LiTS). 2019.

44. Heller N, Sathianathen N, Kalapara A, Walczak E, Moore K, Kaluzniak H, et al. The kits19 challenge data: 300 kidney tumor cases with clinical context, ct semantic segmentations, and surgical outcomes. arXiv preprint arXiv:190400445. 2019.

45. Rister B, Yi D, Shivakumar K, Nobashi T, Rubin DL. CT-ORG, a new dataset for multiple organ segmentation in computed tomography. Sci Data. 2020;7(1):381.

46. Antonelli M, Reinke A, Bakas S, Farahani K, Kopp-Schneider A, Landman BA, et al. The Medical Segmentation Decathlon. Nature communications. 2022;13(1):4128.

47. Sekuboyina A, Husseini ME, Bayat A, Loffler M, Liebl H, Li H, et al. VerSe: A Vertebrae labelling and segmentation benchmark for multi-detector CT images. Medical image analysis. 2021;73:102166.

48. Jordan P, Adamson PM, Bhattbhatt V, Beriwal S, Shen S, Radermecker O, et al. Pediatric chest-abdomen-pelvis and abdomen-pelvis CT images with expert organ contours. Med Phys. 2022;49(5):3523-8.

49. Salimi Y, Shiri I, Akhavanallaf A, Mansouri Z, Sanaat A, Pakbin M, et al. Deep Learning-based calculation of patient size and attenuation surrogates from localizer Image: Toward personalized chest CT protocol optimization. European Journal of Radiology. 2022;157:110602.

50. Salimi Y, Shiri I, Akavanallaf A, Mansouri Z, Arabi H, Zaidi H. Fully automated accurate patient positioning in computed tomography using anterior-posterior localizer images and a deep neural network: a dual-center study. Eur Radiol. 2023:1-10.

51. Shiri I, Vafaei Sadr A, Akhavan A, Salimi Y, Sanaat A, Amini M, et al. Decentralized collaborative multi-institutional PET attenuation and scatter correction using federated deep learning. European Journal of Nuclear Medicine and Molecular Imaging. 2022;In press

52. Qin X, Zhang Z, Huang C, Dehghan M, Zaiane OR, Jagersand M. U2-Net: Going deeper with nested U-structure for salient object detection. Pattern Recognition. 2020;106:107404.

53. Zaker N, Kotasidis F, Garibotto V, Zaidi H. Assessment of Lesion Detectability in Dynamic Whole-Body PET Imaging Using Compartmental and Patlak Parametric Mapping. Clin Nucl Med. 2020;45(5):e221-e31.

54. Fahrni G, Karakatsanis N, Di Domenicantonio G, Garibotto V, Zaidi H. Does whole-body Patlak 18F-FDG PET imaging improve lesion detectability in clinical oncology? Eur Radiol. 2019;29(9):4812-21.

55. Schneider W, Bortfeld T, Schlegel W. Correlation between CT numbers and tissue parameters needed for Monte Carlo simulations of clinical dose distributions. Phys Med Biol. 2000;45(2):459.

56. Waters LS. MCNPX user's manual. Los Alamos Nat Lab. 2002.

57. Jan S, Comtat C, Strul D, Santin G, Trebossen R. Monte Carlo simulation for the ECAT EXACT HR+ system using GATE. IEEE Trans Nucl Sci. 2005;52(3):627-33.

58. Li W, Wang G, Fidon L, Ourselin S, Cardoso MJ, Vercauteren T. On the compactness, efficiency, and representation of 3D convolutional networks: brain parcellation as a pretext task. International conference on information processing in medical imaging. 2017:348-60.

59. Hubbell JH, Seltzer SM. Tables of X-ray mass attenuation coefficients and mass energy-absorption coefficients 1 keV to 20 MeV for elements Z= 1 to 92 and 48 additional substances of dosimetric interest. National Inst. of Standards and Technology-PL. Gaithersburg; 1995.

60. Stabin MG, Sparks RB, Crowe E. OLINDA/EXM: The second-generation personal computer software for internal dose assessment in nuclear medicine. J Nucl Med. 2005;46(6):1023-7.

61. Lee MS, Hwang D, Kim JH, Lee JS. Deep-dose: a voxel dose estimation method using deep convolutional neural network for personalized internal dosimetry. Sci Rep. 2019;9(1):10308.

62. Lee MS, Kim JH, Paeng JC, Kang KW, Jeong JM, Lee DS, et al. Whole-Body Voxel-Based Personalized Dosimetry: The Multiple Voxel S-Value Approach for Heterogeneous Media with Nonuniform Activity Distributions. J Nucl Med. 2018;59(7):1133-9.

63. Schneider W, Bortfeld T, Schlegel W. Correlation between CT numbers and tissue parameters needed for Monte Carlo simulations of clinical dose distributions. Phys Med Biol. 2000;45(2):459-78.

64. Akhavanallaf A, Xie T, Zaidi H. Assessment of uncertainties associated with Monte Carlo-based personalized dosimetry in clinical CT examinations. Phys Med Biol. 2020;65(4):045008.

65. Hendricks JS, McKinney GW, Fensin ML, James MR, Johns RC, et al. MCNPX, Extensions 2.6.0. Los Alamos, NM: Los Alamos National Laboratory, NM; 2008. Report No.: LA-UR-08-2216.

66. Low DA, Harms WB, Mutic S, Purdy JA. A technique for the quantitative evaluation of dose distributions. Med Phys. 1998;25(5):656-61.